GOALS-JWST: Unveiling Dusty Compact Sources in the Merging Galaxy IIZw096

The Astrophysical Journal Letters, 940:L6 (7pp), 2022 November 20 https://doi.org/10.3847/2041-8213/ac9389

GOALS-JWST: Unveiling Dusty Compact Sources in the Merging Galaxy IIZw096

Hanae Inami[1], Jason Surace[2], Lee Armus[2], Aaron S. Evans[3,4], Kirsten L. Larson[5], Loreto Barcos-Munoz[3,4], Sabrina Stierwalt[6], Joseph M. Mazzarella[2], George C. Privon[3,7], Yiqing Song[3,4], Sean T. Linden[8], Christopher C. Hayward[9], Torsten Böker[10], Vivian U[11], Thomas Bohn[1], Vassilis Charmandaris[12,13,14], Tanio Diaz-Santos[13,14], Justin H. Howell[2], Thomas Lai[2], Anne M. Medling[15,16], Jeffrey A. Rich[17], Susanne Aalto[18], Philip Appleton[2], Michael J. I. Brown[19], Shunshi Hoshioka[1], Kazushi Iwasawa[20,21], Francisca Kemper[22,23,24], David Law[25], Matthew A. Malkan[26], Jason Marshall[27], Eric J. Murphy[3], David Sanders[28], and Paul van der Werf[29]
[1] Hiroshima Astrophysical Science Center, Hiroshima University, 1-3-1 Kagamiyama, Higashi-Hiroshima, Hiroshima 739-8526, Japan; hanae@hiroshima-u.ac.jp
[2] IPAC, California Institute of Technology, 1200 East California Boulevard, Pasadena, CA 91125, USA
[3] National Radio Astronomy Observatory, 520 Edgemont Road, Charlottesville, VA 22903, USA
[4] Department of Astronomy, University of Virginia, 530 McCormick Road, Charlottesville, VA 22903, USA
[5] AURA for the European Space Agency (ESA), Space Telescope Science Institute, 3700 San Martin Drive, Baltimore, MD, 21218, USA
[6] Occidental College, Physics Department, 1600 Campus Road, Los Angeles, CA 90042, USA
[7] Department of Astronomy, University of Florida, P.O. Box 112055, Gainesville, FL 32611, USA
[8] Department of Astronomy, University of Massachusetts at Amherst, Amherst, MA 01003, USA
[9] Center for Computational Astrophysics, Flatiron Institute, 162 Fifth Avenue, New York, NY 10010, USA
[10] European Space Agency, Space Telescope Science Institute, Baltimore, Maryland, USA
[11] Department of Physics and Astronomy, 4129 Frederick Reines Hall, University of California, Irvine, CA 92697, USA
[12] Department of Physics, University of Crete, Heraklion, 71003, Greece
[13] Institute of Astrophysics, Foundation for Research and Technology-Hellas (FORTH), Heraklion, 70013, Greece
[14] School of Sciences, European University Cyprus, Diogenes Street, Engomi, 1516 Nicosia, Cyprus
[15] Department of Physics & Astronomy and Ritter Astrophysical Research Center, University of Toledo, Toledo, OH 43606, USA
[16] ARC Centre of Excellence for All Sky Astrophysics in 3 Dimensions (ASTRO 3D), Australia
[17] The Observatories of the Carnegie Institution for Science, 813 Santa Barbara Street, Pasadena, CA 91101, USA
[18] Department of Space, Earth and Environment, Chalmers University of Technology, SE-412 96 Gothenburg, Sweden
[19] School of Physics & Astronomy, Monash University, Clayton, VIC 3800, Australia
[20] Institut de Ciències del Cosmos (ICCUB), Universitat de Barcelona (IEEC-UB), Martí i Franquès, 1, E-08028 Barcelona, Spain
[21] ICREA, Pg. Lluís Companys 23, E-08010 Barcelona, Spain
[22] Institut de Ciencies de l'Espai (ICE, CSIC), Can Magrans, s/n, E-08193 Bellaterra, Barcelona, Spain
[23] ICREA, Pg. Lluś Companys 23, Barcelona, Spain
[24] Institut d'Estudis Espacials de Catalunya (IEEC), E-08034 Barcelona, Spain
[25] Space Telescope Science Institute, 3700 San Martin Drive, Baltimore, MD 21218, USA
[26] Department of Physics & Astronomy, UCLA, Los Angeles, CA 90095-1547, USA
[27] Glendale Community College, 1500 N. Verdugo Road, Glendale, CA 91208, USA
[28] Institute for Astronomy, University of Hawaii, 2680 Woodlawn Drive, Honolulu, HI 96822, USA
[29] Leiden Observatory, Leiden University, NL-2300 RA Leiden, The Netherlands
Received 2022 August 20; revised 2022 September 20; accepted 2022 September 20; published 2022 November 15

Abstract

We have used the Mid-InfraRed Instrument (MIRI) on the James Webb Space Telescope (JWST) to obtain the first spatially resolved, mid-infrared images of IIZw096, a merging luminous infrared galaxy (LIRG) at $z = 0.036$. Previous observations with the Spitzer Space Telescope suggested that the vast majority of the total IR luminosity ($L_{\rm IR}$) of the system originated from a small region outside of the two merging nuclei. New observations with JWST/MIRI now allow an accurate measurement of the location and luminosity density of the source that is responsible for the bulk of the IR emission. We estimate that 40%–70% of the IR bolometric luminosity, or $3–5 \times 10^{11}\,L_{\odot}$, arises from a source no larger than 175 pc in radius, suggesting a luminosity density of at least $3–5 \times 10^{12}\,L_{\odot}\,{\rm kpc}^{-2}$. In addition, we detect 11 other star-forming sources, five of which were previously unknown. The MIRI F1500W/F560W colors of most of these sources, including the source responsible for the bulk of the far-IR emission, are much redder than the nuclei of local LIRGs. These observations reveal the power of JWST to disentangle the complex regions at the hearts of merging, dusty galaxies.

Unified Astronomy Thesaurus concepts: Luminous infrared galaxies (946); Galaxy mergers (608); Infrared astronomy (786); Infrared sources (793)

1. Introduction

IIZw096 (CGCG448-020, IRAS20550+1656) is a merging, luminous infrared galaxy (LIRG) at $z = 0.0361$ with an infrared (IR) luminosity of $L_{\rm IR,8-1000\mu m} = 8.7 \times 10^{11}\,L_{\odot}$, one of the more than 200 LIRGs in the Great Observatories All-sky LIRGs Survey (GOALS; Armus et al. 2009). Previous imaging with the Spitzer Space Telescope revealed that the majority (up to 80%) of the IR luminosity of the entire system comes from a region outside of the merging nuclei (Inami et al. 2010), making it an even more extreme case than the well known Antennae Galaxies (Mirabel et al. 1998; Brandl et al. 2009).

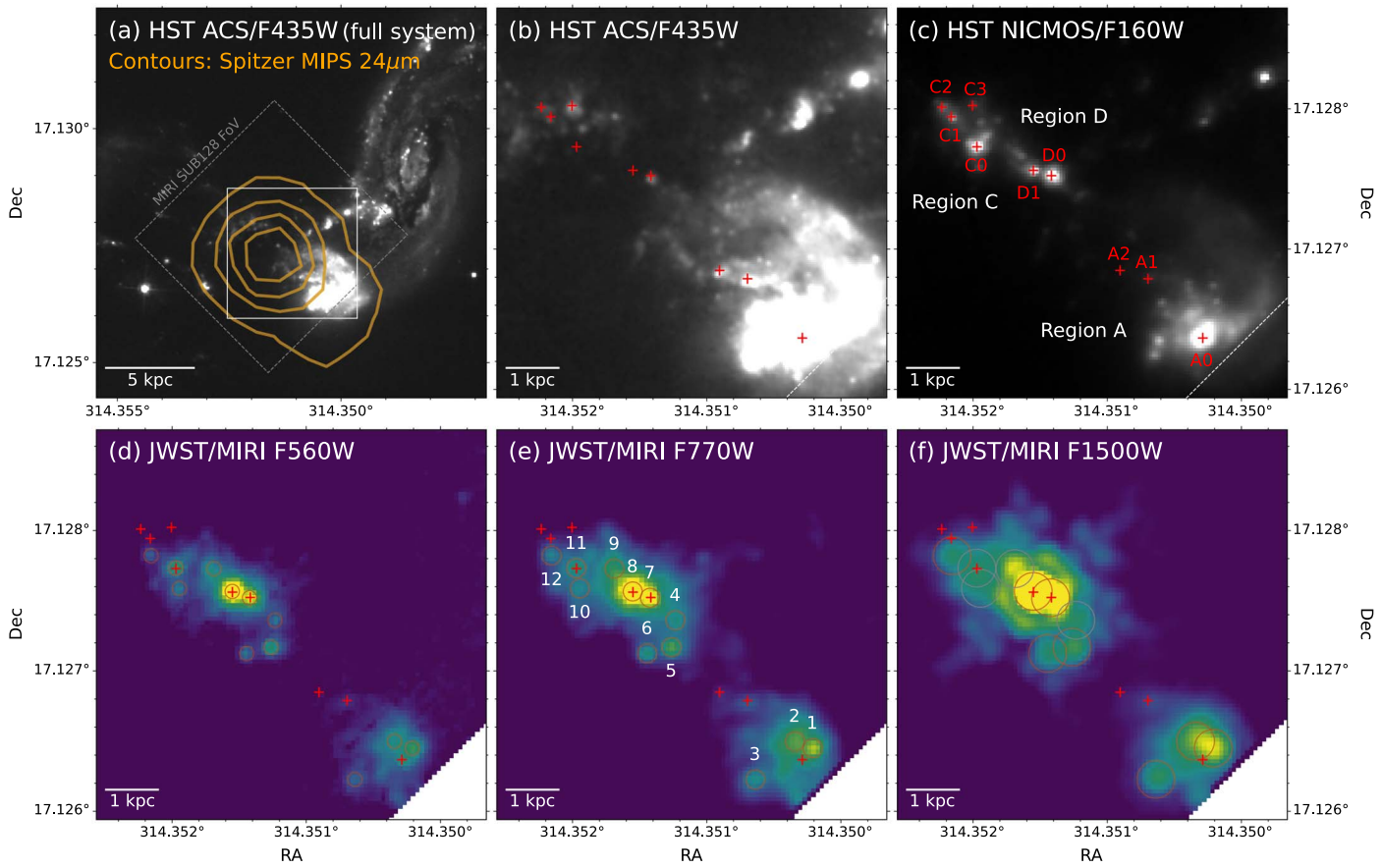

Figure 1. Multiband imaging of IIZw096. (a) HST/Advanced Camera for Surveys (ACS) F435W (0.4 μm) image showing the entire IIZw096 system with Spitzer/MIPS 24 μm contours in orange. The FOV of the JWST/MIRI SUB128 subarray is centered on the dust-obscured region (gray dotted box). The white box indicates the region presented in the rest of the panels. (b) A zoomed-in image of panel (a) showing the obscured region. The red plus symbols are a subset of the sources identified by Wu et al. (2022). (c) HST/NICMOS F160W (1.6 μm) image of the obscured region. The region and source names from Goldader et al. (1997) and Wu et al. (2022), respectively, are shown. (d)–(f) JWST/MIRI SUB128 images taken with the F560W (5.6 μm), F770W (7.7 μm), and F1500W (15 μm) filters. The MIRI images are shown with a logarithmic scale. The red circles indicate the locations of the detected sources with a size corresponding to the beam FWHM. Gray circles indicate sources detected in F560W and F770W but not confidently detected at F1500W. The red plus symbols are the sources detected with HST as shown in panels (b) and (c). PSF features are visible extending outwards from ID 8 in panel (f) because it is compact and bright. All images are shown with north up and east to the left. These images show that while the complexity of IIZw096 was evident from the near-IR HST data, the true nature of the dust emission and the source of the power is only finally revealed with JWST.

The system consists of regions A, C, and D (Figure 1(c)) along with a merging spiral galaxy to the northwest (Goldader et al. 1997). Regions C and D are not detected or have extremely low signal-to-noise ratios (S/Ns) at ultraviolet and optical wavelengths with the Hubble Space Telescope (HST), but only at near-IR and longer wavelengths (Inami et al. 2010; Barcos-Munoz et al. 2017; Wu et al. 2022; Song et al. 2022). Although the Spitzer/MIPS 24 μm image suggested that a single compact source in region D dominates the emission, the large beam size made it impossible to resolve the exact location of the immense far-IR emission. The superior sensitivity and resolving power of the James Webb Space Telescope (JWST) lets us pinpoint the source that is responsible for the intense IR emission and study its complex environment on sub-kpc scales in the mid-IR for the first time.

Here, we present high spatial resolution mid-IR imaging of IIZw096 taken with the JWST Mid-InfraRed Instrument (MIRI; Rieke et al. 2015; Bouchet et al. 2015). Throughout this paper, we adopt a cosmology with $H = 70\,\mathrm{km\,s^{-1}\,Mpc^{-1}}$, $\Omega_\mathrm{M} = 0.28$, and $\Omega_\Lambda = 0.72$. The redshift of IIZw096 ($z = 0.0361$) corresponds to a luminosity distance of 160 Mpc and a projected physical scale of 725 pc arcsec^{-1}.

2. Observations and Data Reduction

The JWST observations were performed under the Directors Discretionary Time Early Release Science (ERS) program 1328 (co-PIs: L. Armus and A.S. Evans). Images of IIZw096 were obtained on 2022 July 2 with a MIRI subarray (SUB128) using the F560W ($\lambda_0 = 5.6\,\mu$m), F770W (7.7 μm), and F1500W (15 μm) filters. The pointing was centered at 314.°35167, 17.°12769 (J2000), where the prominent mid-IR emission was identified with Spitzer. The observations were dithered and the exposure times set to avoid saturation (46, 48, and 48 s, respectively). The data were reduced with the standard JWST calibration pipeline (data processing software ver.2022_2a, calibration software ver.1.5.3; Gordon et al. 2015; Bushouse et al. 2022) and up-to-date reference files from the Calibration References Data System. The images in this work, including HST, are aligned to the Gaia Data Release 3 catalog (Gaia Collaboration et al. 2016, 2021).

3. Results

The $\sim$10$\times$ improvement in the spatial resolution of JWST compared to Spitzer resolves the mid-IR emission into individual clumps down to scales of $\lesssim$100–200 pc, enabling

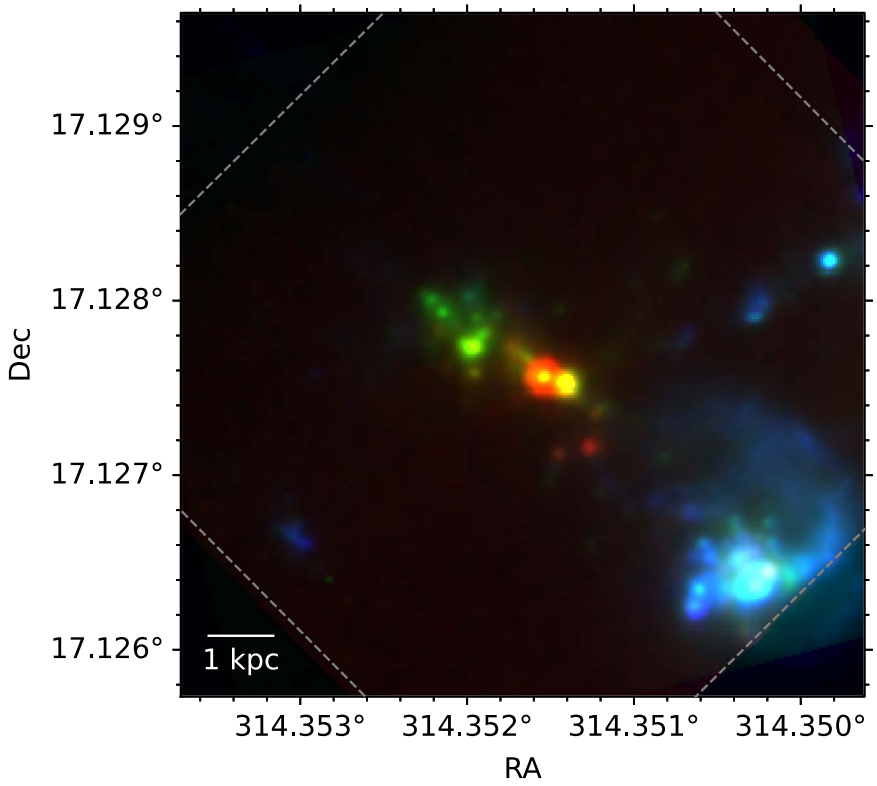

Figure 2. False color image of the IIZw096 obscured region, made with JWST/MIRI F560W (5.6 μm, red), HST/NICMOS F160W (1.6 μm, green), and HST/ACS F435W (0.4 μm, blue). The displayed region is the same as in panels (b)–(f) of Figure 1.

measurements of the mid-IR color and L_{IR} surface density to study the nature of IIZw096.

3.1. Mid-IR Clumps in the Disturbed Region

Individual sources are identified with the `DAOFIND` algorithm (Stetson 1987) in the F770W SUB128 subarray image, which have the highest S/N, using the `Python photutils` package (Bradley et al. 2021). The detection threshold is 5σ. The sources detected in the F770W image are used as priors for photometry in all three bands (Figure 1). We assign identification (ID) numbers for the detected sources in ascending order of R.A. For a subset of sources shown by Wu et al. (2022), we also refer to their source names (Figure 1(c)). The same 12 clumps are detected in the F560W image, while in the F1500W image, four of them (IDs 4, 9, 10, and 11/C0) lie on the structure of the point-spread function (PSF) of the brightest source (ID 8/D1), making confident detections and flux measurements difficult. Thus, we only report their upper limits.

As shown in Figure 1, the most prominent mid-IR source is ID 8 (source D1), lying 0.″47 northeast of ID 7 (source D0). Although ID 8 is fainter than ID 7 in the HST/NICMOS 1.6 μm image, its emission exceeds ID 7 at 5.6 μm and 7.7 μm by a factor of three. At 15 μm, the ID 8-to-ID 7 flux ratio increases to about five. Although ID 7 was previously speculated to be associated with the bulk of the total IR emission due to its prominence at 1.6 μm (Inami et al. 2010), the majority of the mid-IR emission in fact originates from ID 8.

There are five bright mid-IR clumps (IDs 1, 4, 5, 6, and 12) that are either not detected or have an extremely low S/N in the HST 1.6 μm image. ID 1 is in the less dusty region A to the southwest. Three sources, IDs 4, 5, and 6, are south of ID 7. The remaining one, ID 12, is located 2.″27 northeast of ID 8. Interestingly, these new mid-IR selected sources are not concentrated in the dustiest region, but spread throughout the perturbed region.

Additional structure is evident in the MIRI image, outside of the main power source in the IIZw096 system (Figure 2). Region A, which accounts for most of the optical emission, hosts a number of clumps in the MIRI data. Around region C, the emission peaks at 1.6 μm but fades toward the mid-IR.

3.2. Mid-IR Colors of the Clumps

Aperture photometry was employed to measure the fluxes of the detected clumps, except for IDs 7 and 8 due to their relative proximity (see below). The aperture radii used for F560W, F770W, and F1500W are 0.″27, 0.″28, and 0.″30, respectively, with aperture corrections of 0.65, 0.65, and 0.50.[30] Aperture photometry in the F1500W image was performed after subtracting ID 8, due to its prominent PSF pattern (note that the PSF has not been subtracted in Figure 1(f)). The source subtraction was performed using a PSF generated by `WebbPSF` (Perrin et al. 2012, 2014).[31] To account for the extremely red color of ID 8, a power-law spectrum with a spectral slope of 3, resembling the mid-IR color of IIZw096, was used to generate the PSF. This provides a more accurate flux measurement of the sources around ID 8.

To extract the fluxes of IDs 7 and 8, a simultaneous two-dimensional Gaussian fit was performed in the F560W and F770W images. In the F1500W image, the flux of ID 8, which

[30] The aperture correction values are from the PSF encircled energy at https://jwst-docs.stsci.edu/jwst-mid-infrared-instrument/miri-performance/miri-point-spread-functions.

[31] https://www.stsci.edu/jwst/science-planning/proposal-planning-toolbox/psf-simulation-tool

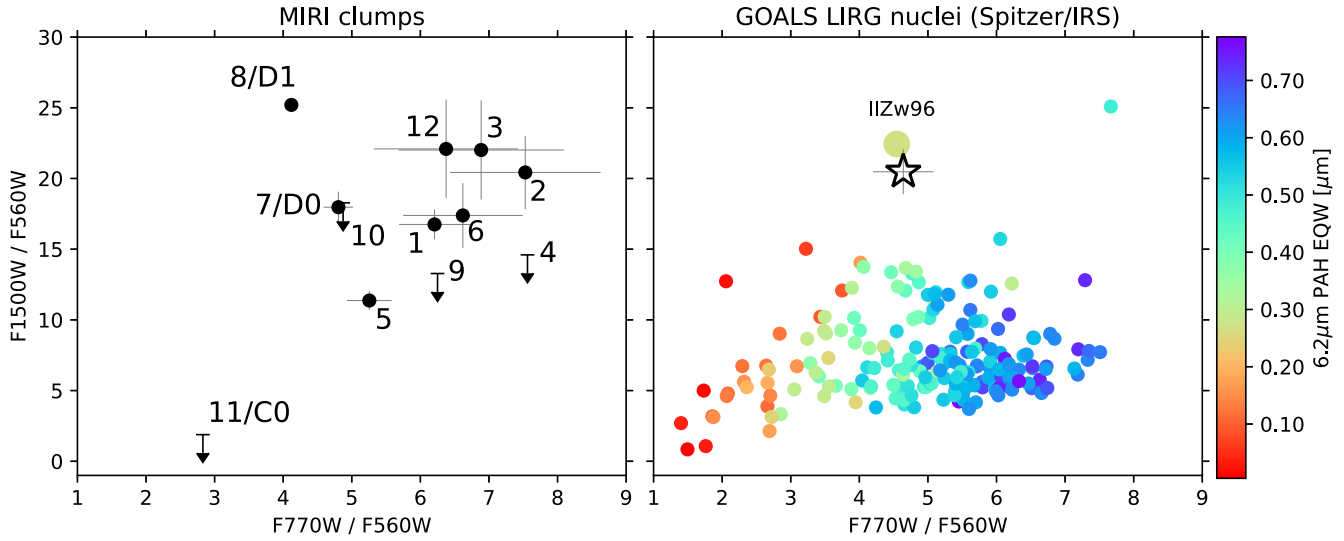

Figure 3. Left: F1500W/F560W−F770W/F560W color–color diagram for all clumps detected in the MIRI images. For sources without a detection in the F1500W image, upper limits are indicated by downward arrows. Right: for comparison, the same diagram but showing the colors of local LIRG nuclei derived from synthetic photometry of the Spitzer/IRS low-resolution spectra. The data points are color-coded by the 6.2 μm PAH EQW measured from the spectra. The color derived from the total flux of the MIRI clumps in the left panel is shown as a star. In the Spitzer slit that covers the merger-induced dusty region, IIZw096 has one of the reddest F1500W/F560W colors among local LIRGs.

Table 1
Flux Density of the Clumps Detected in F560W, F770W, and F1500W

ID	R.A. degree	Decl. degree	F560W mJy	F770W mJy	F1500W mJy
1	314.350210	17.126449	$0.51^{+0.03}_{-0.03}$	$3.17^{+0.16}_{-0.23}$	$8.56^{+0.30}_{-0.18}$
2	314.350342	17.126498	$0.35^{+0.03}_{-0.05}$	$2.62^{+0.17}_{-0.27}$	$7.10^{+0.36}_{-0.25}$
3	314.350638	17.126226	$0.13^{+0.03}_{-0.01}$	$0.87^{+0.06}_{-0.08}$	$2.79^{+0.14}_{-0.09}$
4	314.351233	17.127361	$0.13^{+0.03}_{-0.02}$	$0.97^{+0.05}_{-0.15}$	<1.87
5	314.351263	17.127169	$0.30^{+0.02}_{-0.01}$	$1.60^{+0.05}_{-0.06}$	$3.46^{+0.18}_{-0.03}$
6	314.351444	17.127124	$0.13^{+0.03}_{-0.01}$	$0.86^{+0.03}_{-0.04}$	$2.27^{+0.13}_{-0.04}$
7/D0	314.351423	17.127521	$1.79^{+0.05}_{-0.05}$	$8.60^{+0.30}_{-0.30}$	$32.16^{+1.74}_{-1.74}$
8/D1	314.351552	17.127566	$6.17^{+0.04}_{-0.04}$	$25.40^{+0.21}_{-0.21}$	$155.39^{+1.62}_{-1.62}$
9	314.351688	17.127728	$0.31^{+0.04}_{-0.03}$	$1.91^{+0.14}_{-0.19}$	<4.07
10	314.351945	17.127588	$0.15^{+0.03}_{-0.02}$	$0.75^{+0.09}_{-0.18}$	<2.80
11/C0	314.351972	17.127732	$0.39^{+0.02}_{-0.03}$	$1.09^{+0.08}_{-0.18}$	<0.73
12	314.352156	17.127821	$0.11^{+0.02}_{-0.01}$	$0.67^{+0.04}_{-0.05}$	$2.33^{+0.14}_{-0.07}$
Total			$10.45^{+0.36}_{-0.33}$	$48.52^{+1.39}_{-1.94}$	$214.06^{+4.63}_{-4.04}$

dominates the emission, was also extracted via a simultaneous two-dimensional Gaussian fit. However, we did not adopt the flux of ID 7 from this fit because this source lies on the Airy ring of ID 8. Instead, the flux of ID 7 was derived from a single Gaussian fit[32] to the image after subtraction of ID 8 to minimize contamination from the PSF.

The local background was measured using a 3σ-clipped median of various annuli. They have a minimum inner radius 2.4× the half-width at half-maximum (HWHM) of the PSF and a maximum radius that is 14× (for F560W and F770W) and 7× (F1500W) the PSF HWHM in steps of 0.″05 around each source. During this process, the other detected sources were masked out to avoid background overestimation. Each of the measured background levels was separately subtracted from the measured flux, providing a distribution of fluxes for each source. The median value of this distribution is reported as the final flux density in Table 1. The 16th and 84th percentiles were adopted as the flux uncertainties.

Based on the measured fluxes in all three MIRI bands, we show a F1500W/F560W−F770W/F560W color–color diagram in Figure 3. These colors are a sensitive measure of the mid-IR continuum slope, and the F770W/F560W color is also sensitive to emission of polycyclic aromatic hydrocarbon (PAH) at 7.7 μm. The individual clumps detected in the MIRI SUB128 images are shown in the left panel. We also present the same diagram for local LIRG nuclei using Spitzer/IRS low-resolution spectra taken with Short-Low (SL; 5.5–14.5 μm) and Long-Low (LL; 14−38 μm) spectroscopy (Stierwalt et al. 2013, 2014). We generated synthetic photometry from the spectra using the MIRI filter curves and the `Python synphot` package (STScI Development Team 2018). The SL and LL slits fully cover regions C and D. The LL slit also covers region A. As expected from the IRS spectra (Inami et al. 2010; Stierwalt et al. 2013), the F1500W/F560W color from the

[32] We adopted Gaussian fits for IDs 7 and 8 to use a consistent method across the filter bands.

synthetic photometry of the dust-obscured region in IIZw096 is an outlier with a much redder color than the rest of the local LIRGs. With JWST/MIRI, we are now able to decompose the emission into individual clumps to study the distribution of their mid-IR colors.

The summed flux of all the clumps in color space agrees well with the color measured with the much larger beam of Spitzer/IRS (Figure 3 right). All MIRI-detected clumps show redder colors (F1500W/F560W $\gtrsim 15$) than most of the local LIRG nuclei, except for ID 5, which has F1500W/F560W $= 11 \pm 0.7$. ID 8 (D1) is the reddest, while ID 7 (D0) has a comparable F1500W/F560W color to the other clumps. The newly detected source ID 12 is the second reddest, along with IDs 2 and 3 having excess emission at 15 μm and 7.7 μm compared to most of the other sources.

The F770W/F560W colors of the clumps are spread over the range $4 \lesssim$ F770W/F560W $\lesssim 8$. As expected, since they dominate the mid-IR flux, the F770W/F560W colors of the two brightest sources, IDs 7 and 8, agree well with the color of IIZw096 derived from the synthetic photometry of the IRS spectrum. The remaining sources, except for IDs 5, 10, and 11, are redder, with F770W/F560W $\gtrsim 6$. These red sources have F770W/F560W colors consistent with strong PAH emission. The bluer sources suggest weaker PAH emission or an excess of hot dust. The F770W/F560W colors of IDs 7 and 8 are comparable to sources with 6.2 μm PAH equivalent widths (EQWs) of about half those seen in pure starburst nuclei (Figure 3 right), which are consistent with the direct measurement in the IRS spectrum (6.2 μm PAH EQW $= 0.26$ μm; Inami et al. 2010) and may indicate an excess of very hot dust.

3.3. IR Luminosity Surface Density

To estimate the luminosity density of each clump in the MIRI image, we first use the measured flux to estimate $L_{\rm IR}$. Assuming that the 15 μm flux correlates with $L_{\rm IR}$, we compute the fractional contribution of each clump to the total 15 μm flux. The flux of the diffuse emission is measured with an aperture of radius 7″ centered on the F1500W image with the total flux of all the clumps being subtracted. The resulting flux density of the diffuse emission is 190 mJy.[33] Finally, the $L_{\rm IR}$ estimated in the obscured region ($6.87 \times 10^{11}\,L_{\odot}$; Inami et al. 2010) is scaled by these fractions to calculate the $L_{\rm IR}$ of each component. The resulting $L_{\rm IR}$ for ID 8 (D1) is $3 \times 10^{11}\,L_{\odot}$, corresponding to a star formation rate (SFR) of $40\,M_{\odot}\,{\rm yr}^{-1}$ (assuming a Kroupa initial mass function; Kennicutt 1998; Kroupa 2001; Madau & Dickinson 2014). This rises to $5 \times 10^{11}\,L_{\odot}$ or a SFR of $60\,M_{\odot}\,{\rm yr}^{-1}$ if we assume that the diffuse emission at 15 μm does not contribute to $L_{\rm IR}$ at all, because this ascribes more of the $L_{\rm IR}$ to ID 8.

As an alternative, we derive a bolometric correction factor from the ensemble of GOALS nuclei to estimate the $L_{\rm IR}$ of each clump. This factor is calculated using the 29 GOALS nuclei with similar colors to the clumps in IIZw096, i.e., F1500W/F560W > 10 and F770W/F560W > 4 shown in Figure 3 (right). From this we obtain a median bolometric correction factor ($L_{\rm IR}/L_{\nu}(15_{\mu{\rm m}})$) of 4 ± 3. This yields $L_{\rm IR} = (5 \pm 4) \times 10^{11}\,L_{\odot}$ for ID 8 (D1). This is consistent with the $L_{\rm IR}$ estimate above, where the total $L_{\rm IR}$ in the dust-embedded region is split up based on the 15 μm flux fraction of each clump.

We can also estimate $L_{\rm IR}$ based on the known correlation between the 8 μm luminosity (L_8) and $L_{\rm IR}$ ($L_{\rm IR}/L_8 = 4.9^{+2.9}_{-2.2}$; Elbaz et al. 2011). However, L_8 for this correlation was obtained using the Spitzer 8 μm band, which has a wider bandwidth than JWST/F770W (2.9 μm and 2.2 μm, respectively). Assuming that the bandwidth ratio can be used to correct for this difference, we obtain $L_{\rm IR} = (2 \pm 1) \times 10^{11}\,L_{\odot}$ for ID 8. This 8 μm-based $L_{\rm IR}$ is slightly lower than, but consistent with the 15 μm-based $L_{\rm IR}$. Because the longer IR wavelength better traces the IR bolometric luminosity, we adopt the 15 μm-based $L_{\rm IR}$ hereafter.

Because ID 8 (D1) is unresolved, the MIRI PSF size at 15 μm limits its radius to $<$175 pc. Thus, a lower limit on the $L_{\rm IR}$ surface density ($\Sigma L_{\rm IR}$) is >3–$5 \times 10^{12}\,L_{\odot}\,{\rm kpc}^{-2}$. This corresponds to a SFR surface density of $>$400–600 $M_{\odot}\,{\rm yr}^{-1}\,{\rm kpc}^{-2}$ if powered by star formation.

4. Discussion

Our JWST imaging has revealed the complexity of the dustiest region of the merging galaxy, IIZw096. The three main components in the perturbed region show a wide variety of optical–IR colors and morphologies, with a mix of bright, unresolved clumps and diffuse emission. This suggests a range in properties, such as extinction, SFR, age, and dust temperature in this ongoing merger.

Although ID 7 (D0) is the brightest source at 1.6 μm, the JWST mid-IR data demonstrate that ID 8 (D1) generates the bulk of the total IR emission in IIZw096. The location of ID 8 also coincides with two OH megamasers (Migenes et al. 2011; Wu et al. 2022).[34] Megamasers are often found in merging (U)LIRGs, in close proximity to the nuclei (e.g., Roberts et al. 2021), marking regions of extremely high gas density and strong far-IR radiation.

The emission we have targeted with JWST is clearly responsible for the bulk of the luminosity in IIZw096 and it arises from outside of the prominent two merging galaxies, one of which is the spiral galaxy to the northwest that lies outside of the MIRI SUB128 field of view (FOV) (Figure 1(a)). However, it is possible that ID 8 is a third nucleus in this system. Given the observed mid-IR morphology, region A + C + D could be a single disrupted galaxy or it could be two galaxies with source A0 being one nucleus and ID 8 (D1) being the other. The diffuse, extended emission around ID 8 would then be the remnants of the third galaxy's disk. The estimated stellar mass of ID 8 is $\sim 10^9\,M_{\odot}$ and there is a similarly large mass of gas in this region (Inami et al. 2010; Wu et al. 2022). These estimates might indicate ID 8 is a partially stripped third nucleus. Although the current MIRI SUB128 images do not provide evidence for either the two- or three-body merger scenario, our upcoming JWST observations (ERS program 1328) may elucidate this question. The deeper MIRI and NIRCam full-array imaging may detect a more pronounced disk-like morphology around ID 8. A detection of a rotation curve around ID 8 by the planned spectroscopic observations could suggest that ID 8 is a third nucleus.

ID 8 (D1) generates 40%–70% of the total IR emission of the IIZw096 system, corresponding to an $L_{\rm IR}$ surface density of >3–$5 \times 10^{12}\,L_{\odot}\,{\rm kpc}^{-2}$. This is $\sim 10\times$ the characteristic surface

[33] In F560W and F770W, diffuse emission fluxes measured with the same method are 18mJy and 90mJy, respectively.

[34] IIZw096 also hosts an H_2O megamaser (Wiggins et al. 2016; Kuo et al. 2018), but its exact location is unknown.

brightness of starbursts, but comparable to super star clusters (Meurer et al. 1997) including some in the Antennae Galaxies (Brandl et al. 2009). The $L_{\rm IR}$ surface density limit of ID 8 is also consistent with the ULIRG nuclei studied at 12.5 μm with Keck (Soifer et al. 2000, 2001). In addition, the 33 GHz continuum imaging (0.″1 resolution) taken with the Very Large Array shows that the peak emission is located at ID 8 (Song et al. 2022). These authors estimated a SFR surface density of $470 \pm 60\,M_{\odot}\,{\rm yr}^{-1}\,{\rm kpc}^{-2}$, corresponding to an $L_{\rm IR}$ surface density of $(3.9 \pm 0.5) \times 10^{12}\,L_{\odot}\,{\rm kpc}^{-2}$, which agrees with the value derived from the mid-IR. Given the $L_{\rm IR}$ surface density limit from the mid-IR and the column density of $\sim 10^{25}\,{\rm cm}^{-2}$ obtained via the molecular gas mass (within an aperture of $0.''2 \times 0.''16$; Wu et al. 2022), ID 8 appears to be below the Eddington limit if its size is 175 pc. (e.g., Pereira-Santaella et al. 2021; Barcos-Munoz et al. 2015).

The clumps in the disturbed region, including ID 8 (D1), are much redder in F1500W/F560W than local LIRG nuclei. Based on the 9.7 μm silicate optical depth ($\tau_{9.7\mu{\rm m}} \sim 1$) derived from Spitzer/IRS spectroscopy, the V-band extinction is estimated to be $\geqslant$19 mag (Inami et al. 2010). The unusually red colors of IIZw096 could be due to an extremely young, highly obscured starburst or active galactic nucleus (AGN), triggered by the recent merger. The other LIRG with a very red F1500W/F560W color, IRAS22491-1808, is also an ongoing merger with bright clumps of star formation (Surace 1998; Surace et al. 1998).

The F770W/F560W color traces the 7.7 μm PAH emission and is also a good proxy for the 6.2 μm PAH EQW (Figure 3, right). Using the 6.2 μm PAH EQW as a diagnostic of starbursts and AGNs (e.g., Brandl et al. 2006; Armus et al. 2007; Petric et al. 2011), the clumps with F770W/F560W $\gtrsim 5$ are consistent with pure star formation. However, the color of ID 8 (D1) is in the range where an AGN cannot be excluded. Although an analysis of the X-ray spectra of IIZw096 obtained with Chandra, XMM-Newton, and NuSTAR also favors star formation, the non-detection of ID 8 by NuSTAR does not rule out a Compton-thick AGN if the column density exceeds $10^{25}\,{\rm cm}^{-2}$ (Iwasawa et al. 2011; Ricci et al. 2021). In fact, the estimated column density of ID 8 is $\sim 10^{25}\,{\rm cm}^{-2}$ (Wu et al. 2022). The evidence may be consistent with the presence of a Compton-thick AGN but it is equally consistent with a starburst, and neither is conclusive. Our upcoming mid-IR and near-IR spectroscopic data (ERS program 1328) are expected to shed additional light on the underlying energy source of this heavily obscured source, perhaps through detection of one or more coronal emission lines.

5. Conclusions

JWST/MIRI imaging has demonstrated uncharted aspects of the dust emission from the extremely luminous merging galaxy IIZw096. The high spatial resolution and high-sensitivity mid-IR imaging of this work yields the following findings:

1. For the first time, we have spatially resolved the mid-IR emission of the merger-induced heavily dust-obscured region of IIZw096. We identify the source (ID 8/D1) that is responsible for the bulk of the mid-IR emission, accounting for 40%−70% of the total IR emission of the system.
2. In total, 12 clumps are detected in the F770W (and F560W) image, five of which are newly identified and were not detected or had low S/N detections at 1.6 μm with HST/NICMOS. Most of the clumps have similar F1500W/F560W colors, ranging from ∼15 to 25. These colors are about twice as red as local LIRG nuclei, but agree with the colors derived from synthetic photometry of Spitzer spectra of this system. Among LIRG nuclei, the F770W/F560W colors roughly correlate with the 6.2 μm PAH EQW, and therefore the clumps have colors indicative of 6.2 μm PAH EQWs from ∼0.3 μm to 0.6 μm, slightly lower than but including pure star formation.
3. The estimated $L_{\rm IR}$ of ID 8 (D1) is $3–5 \times 10^{11}\,L_{\odot}$, which corresponds to a SFR of 40–60 $M_{\odot}\,{\rm yr}^{-1}$ if it is star forming. As the source is unresolved, we estimate its $L_{\rm IR}$ surface density to be $>3–5 \times 10^{12}\,L_{\odot}\,{\rm kpc}^{-2}$ or a SFR surface density of $>400–600\,M_{\odot}\,{\rm yr}^{-1}\,{\rm kpc}^{-2}$. Such high surface densities put source D1 in a range comparable to young super star clusters and ULIRG nuclei.

The JWST mid-IR imaging described in this *Letter* has revealed a hidden aspect of IIZw096, and has opened a door toward identifying heavily dust-obscured sources which cannot be found at shorter wavelengths. Future planned spectroscopic observations of IIZw096 will provide additional information on the nature of the dust, ionized gas, and warm molecular gas in and around the disturbed region of this luminous merging galaxy.

The authors would like to thank the referee whose constructive comments helped improve the manuscript. The JWST data presented in this paper were obtained from the Mikulski Archive for Space Telescopes (MAST) at the Space Telescope Science Institute. The specific observations analysed can be accessed via https://doi.org/10.17909/8c47-wb74. STScI is operated by the Association of Universities for Research in Astronomy, Inc., under NASA contract NAS526555. Support to MAST for these data is provided by the NASA Office of Space Science via grant NAG57584 and by other grants and contracts. This work is based on observations made with the NASA/ESA/CSA James Webb Space Telescope. These observations are associated with program 1328. The data were obtained from the Mikulski Archive for Space Telescopes at the Space Telescope Science Institute, which is operated by the Association of Universities for Research in Astronomy, Inc., under NASA contract NAS 5-03127 for JWST. This research has made use of the NASA/IPAC Extragalactic Database (NED), which is funded by the National Aeronautics and Space Administration and operated by the California Institute of Technology. H.I. and T.B. acknowledge support from JSPS KAKENHI grant No. JP21H01129 and the Ito Foundation for Promotion of Science. Y.S. is supported by the NSF through grant AST 1816838 and the Grote Reber Fellowship Program administered by the Associated Universities, Inc./ National Radio Astronomy Observatory. The Flatiron Institute is supported by the Simons Foundation. Vivian U acknowledges funding support from NASA Astrophysics Data Analysis Program (ADAP) grant 80NSSC20K0450. A.M.M. acknowledges support from the National Science Foundation under grant No. 2009416. S.A. gratefully acknowledges support from an ERC Advanced grant 789410, from the Swedish Research Council and from the Knut and Alice Wallenberg (KAW) foundation. K.I. acknowledges support by the Spanish MCIN under grant PID2019-105510GB-C33/AEI.

Facilities: JWST (MIRI), HST (ACS, NICMOS) NED.

Software: astropy (Astropy Collaboration et al. 2013, 2018), photutils (Bradley et al. 2021), synphot (STScI Development Team 2018), WebbPSF (Perrin et al. 2012, 2014).

ORCID iDs

Hanae Inami https://orcid.org/0000-0003-4268-0393
Jason Surace https://orcid.org/0000-0001-7291-0087
Lee Armus https://orcid.org/0000-0003-3498-2973
Aaron S. Evans https://orcid.org/0000-0003-2638-1334
Kirsten L. Larson https://orcid.org/0000-0003-3917-6460
Loreto Barcos-Munoz https://orcid.org/0000-0003-0057-8892
Sabrina Stierwalt https://orcid.org/0000-0002-2596-8531
Joseph M. Mazzarella https://orcid.org/0000-0002-8204-8619
George C. Privon https://orcid.org/0000-0003-3474-1125
Yiqing Song https://orcid.org/0000-0002-3139-3041
Sean T. Linden https://orcid.org/0000-0002-1000-6081
Christopher C. Hayward https://orcid.org/0000-0003-4073-3236
Torsten Böker https://orcid.org/0000-0002-5666-7782
Vivian U https://orcid.org/0000-0002-1912-0024
Thomas Bohn https://orcid.org/0000-0002-4375-254X
Vassilis Charmandaris https://orcid.org/0000-0002-2688-1956
Tanio Diaz-Santos https://orcid.org/0000-0003-0699-6083
Justin H. Howell https://orcid.org/0000-0001-6028-8059
Thomas Lai https://orcid.org/0000-0001-8490-6632
Anne M. Medling https://orcid.org/0000-0001-7421-2944
Jeffrey A. Rich https://orcid.org/0000-0002-5807-5078
Susanne Aalto https://orcid.org/0000-0002-5828-7660
Philip Appleton https://orcid.org/0000-0002-7607-8766
Michael J. I. Brown https://orcid.org/0000-0002-1207-9137
Kazushi Iwasawa https://orcid.org/0000-0002-4923-3281
Francisca Kemper https://orcid.org/0000-0003-2743-8240
David Law https://orcid.org/0000-0002-9402-186X
Matthew A. Malkan https://orcid.org/0000-0001-6919-1237
Jason Marshall https://orcid.org/0000-0001-7712-8465
Eric J. Murphy https://orcid.org/0000-0001-7089-7325
David Sanders https://orcid.org/0000-0002-1233-9998
Paul van der Werf https://orcid.org/0000-0001-5434-5942

References

Armus, L., Charmandaris, V., Bernard-Salas, J., et al. 2007, ApJ, 656, 148
Armus, L., Mazzarella, J. M., Evans, A. S., et al. 2009, PASP, 121, 559
Astropy Collaboration, Price-Whelan, A. M., Sipocz, B. M., et al. 2018, AJ, 156, 123
Astropy Collaboration, Robitaille, T. P., Tollerud, E. J., et al. 2013, A&A, 558, A33
Barcos-Munoz, L., Leroy, A. K., Evans, A. S., et al. 2015, ApJ, 799, 10
Barcos-Muñoz, L., Leroy, A. K., Evans, A. S., et al. 2017, ApJ, 843, 117
Bouchet, P., García-Marín, M., Lagage, P.-O., et al. 2015, PASP, 127, 612
Bradley, L., Sipőcz, B., Robitaille, T., et al. 2021, astropy/photutils v1.1.0, Zenodo, doi:10.5281/zenodo.4624996
Brandl, B. R., Bernard-Salas, J., Spoon, H. W. W., et al. 2006, ApJ, 653, 1129
Brandl, B. R., Snijders, L., den Brok, M., et al. 2009, ApJ, 699, 1982
Bushouse, H., Eisenhamer, J., Dencheva, N., et al. 2022, spacetelescope/jwst: JWST v1.6.2, Zenodo, doi:10.5281/zenodo.6984366
Elbaz, D., Dickinson, M., Hwang, H. S., et al. 2011, A&A, 533, A119
Gaia Collaboration, Brown, A. G. A., Vallenari, A., et al. 2021, A&A, 649, A1
Gaia Collaboration, Prusti, T., de Bruijne, J. H. J., et al. 2016, A&A, 595, A1
Goldader, J. D., Goldader, D. L., Joseph, R. D., Doyon, R., & Sanders, D. B. 1997, AJ, 113, 1569
Gordon, K. D., Chen, C. H., Anderson, R. E., et al. 2015, PASP, 127, 696
Inami, H., Armus, L., Surace, J. A., et al. 2010, AJ, 140, 63
Iwasawa, K., Sanders, D. B., Teng, S. H., et al. 2011, A&A, 529, A106
Kennicutt, R. C., Jr. 1998, ApJ, 498, 541
Kroupa, P. 2001, MNRAS, 322, 231
Kuo, C. Y., Constantin, A., Braatz, J. A., et al. 2018, ApJ, 860, 169
Madau, P., & Dickinson, M. 2014, ARA&A, 52, 415
Meurer, G. R., Heckman, T. M., Lehnert, M. D., Leitherer, C., & Lowenthal, J. 1997, AJ, 114, 54
Migenes, V., Coziol, R., Cooprider, K., et al. 2011, MNRAS, 416, 1267
Mirabel, I. F., Vigroux, L., Charmandaris, V., et al. 1998, A&A, 333, L1
Pereira-Santaella, M., Colina, L., García-Burillo, S., et al. 2021, A&A, 651, A42
Perrin, M. D., Sivaramakrishnan, A., Lajoie, C.-P., et al. 2014, Proc. SPIE, 9143, 91433X
Perrin, M. D., Soummer, R., Elliott, E. M., et al. 2012, Proc. SPIE, 8442, 84423D
Petric, A. O., Armus, L., Howell, J., et al. 2011, ApJ, 730, 28
Ricci, C., Privon, G. C., Pfeifle, R. W., et al. 2021, MNRAS, 506, 5935
Rieke, G. H., Wright, G. S., Böker, T., et al. 2015, PASP, 127, 584
Roberts, H., Darling, J., & Baker, A. J. 2021, ApJ, 911, 38
Soifer, B. T., Neugebauer, G., Matthews, K., et al. 2000, AJ, 119, 509
Soifer, B. T., Neugebauer, G., Matthews, K., et al. 2001, AJ, 122, 1213
Song, Y., Linden, S. T., Evans, A. S., et al. 2022, arXiv:2209.04002
Stetson, P. B. 1987, PASP, 99, 191
Stierwalt, S., Armus, L., Surace, J. A., et al. 2013, ApJS, 206, 1
Stierwalt, S., Armus, L., Charmandaris, V., et al. 2014, ApJ, 790, 124
STScI Development Team 2018, synphot: Synthetic photometry using Astropy, Astrophysics Source Code Library, ascl:1811.001
Surace, J. A. 1998, PhD thesis, Univ. of Hawaii, Manoa, Institute for Astronomy
Surace, J. A., Sanders, D. B., Vacca, W. D., Veilleux, S., & Mazzarella, J. M. 1998, ApJ, 492, 116
Wiggins, B. K., Migenes, V., & Smidt, J. M. 2016, ApJ, 816, 55
Wu, H., Wu, Z., Sotnikova, Y., et al. 2022, A&A, 661, A125